COBEM 2021 26th International Congress of Mechanical Engineering
ABCM Associação Brasileira de Engenharia e Ciências Mecânicas
November 22-26, 2021, Virtual Congress, Brazil

COB-2021-0425
NUMERICAL SIMULATION OF VORTEX INDUCED MOTION ON SEMI-SUBMERSIBLE PLATFORM

Daniel Francisconi Oliveira
Department of Naval Arch. & Ocean Eng., Escola Politécnica, University of São Paulo, São Paulo, SP 05508-030, Brazil
daniel.francisconi.oliveira@usp.br

Bruno Souza Carmo
Department of Mechanical Engineering, Escola Politécnica, University of São Paulo, São Paulo, SP 05508-030, Brazil
bruno.carmo@usp.br

Abstract. *Offshore wind technology is a current challenging subject and an essential step to achieve carbon neutrality. One of the most important floating wind systems, OC4-DeepCWind, was designed merging onshore wind technology with oil and gas floating systems. This work analyzes this platform hydrodynamic response under the impact of ocean currents with a 2-D model in 1, 2, and 3 degrees of freedom (DoF) for three different inflow angles (0°, 30°and 60°). Important forces and motions arise from Vortex Induced Motion (VIM), and it was found that the simplified model in a laminar regime (Re=150) has a good agreement with experimental data for higher Reynolds number. In most of the cases a 1-DoF model sufficiently describes the platform dynamics, and it was found that fluid-structure interaction is responsible for angular instabilities if the inflow angle is nonzero. The lock-in ratio frequency between inline and transverse response was found to be different according to the inflow angle.*

Keywords: *vortex-induced motion, semi-submersible platform, computational fluid dynamics, floating offshore wind turbine.*

1. INTRODUCTION

Wind energy onshore is well established, and the new challenge is to apply this technology on the oceans. Although at offshore locations the wind resource is usually better (Esteban *et al.*, 2011), with less obstacles and huge empty areas, engineers must face the problem of waves and current. As the turbines get further from the coast, the depth makes it unfeasible to fix the structure to the ground, so a floating moored system is required, which adds much more complexity to the dynamic motion of turbines. An important consequence of currents around the immersed parts of floating bodies is the Vortex Induced Motion (VIM), when the structure experiences motion due to the alternate loads originated from the shed of vortices, a detailed explanation of the phenomenon can be found in Fujarra *et al.* (2012).

In this work, we investigate one of the most important floating offshore wind turbines available for the research community, the NREL 5MW wind turbine mounted on the semi-submersible floating system OC4 Phase II defined in Robertson *et al.* (2014). The platform consists of 3 columns disposed in a triangular configuration with one smaller main column at the center, on which the turbine tower is mounted. The heave plates and smaller members may have limited effects on the VIM compared to the to the columns, so a two-dimensional computational model should be enough to obtain the structural response with acceptable uncertainty and low computational cost, which is fundamental due to the high number of simulations that are necessary to reach a thorough understanding of the dynamical behaviour of the system.

Simulations with in-plane 3-DoF of the semi-submersible OC4 were conducted in the OpenFOAM software (Weller *et al.*, 1998) with the structure modelled as a single rigid body mounted on an elastic base. Results are compared with experimental and numerical available data, bounding the limits of the 2-D model.

2. CASE STUDY

The semi-submersible platform designed in the Phase II of the Offshore Code Comparison Collaboration Continuation (OC4), the so-called DeepCwind floating wind system, can be visualized in Fig. 1. This design was mainly developed by the U.S. National Renewable Energy Laboratory (NREL) as a project aimed at generating test data for use in validation floating offshore wind turbine modeling tools (Robertson *et al.*, 2014).

The platform consists of 3 outer columns disposed in a triangular configuration with one smaller inner column at the

center, on which the turbine tower is mounted. The outer columns have a diameter of 12 m (Fig. 1b) and the inner column is 6.5 m diameter size (Fig. 1c). The heave plates are the structures below the outer columns built for reducing vertical oscillation along the z direction through drag forces and capable of holding ballast to lower the gravity center and increase pitch and roll stability. In addition, smaller members, such as the cylindrical pontoons or cross braces, play a structural role of connecting all parts.

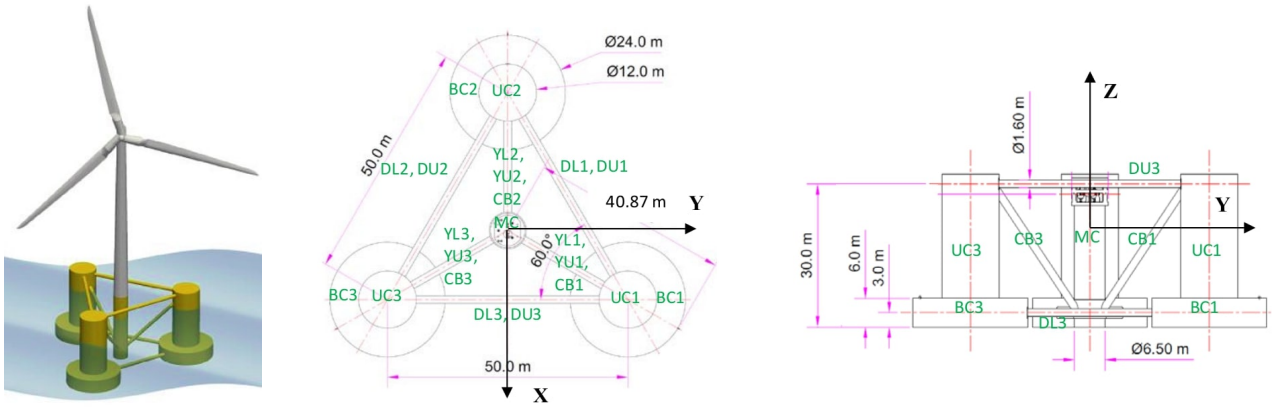

(a) 3D view (Johlas *et al.*, 2021)

(b) Plan view (Robertson *et al.*, 2014)

(c) Side view (Robertson *et al.*, 2014)

Figure 1: OC4 DeepCWind floating wind system design views.

The floating system is usually subjected to hydrodynamic forces from current and waves, as well as loads from the mooring system, structural weight and aerodynamic forces. In this work, we investigate the first one, related to the ocean currents that can be of the order of 1 m/s. We are interested in predicting the dynamic response of a platform subjected to a constant flow velocity.

Thus, when the floating system is submitted to an ocean current, the heave plates and smaller members may have limited effects on the VIM in the x-y plane compared to the columns. Therefore, a two-dimensional computational model should be enough to obtain the dynamic response with acceptable uncertainty and low computational cost, which is fundamental due to the high number of simulations that are necessary to reach a thorough understanding of the dynamical behaviour of the system. The 2-D model geometry is shown in Fig. 2. As the dimensions are less important than the dimensionless numbers of the problem, the model is a 1:12 representation of the original dimensions of the platform, in such a way the outer columns have a unitary diameter $D_{out} = 1\,\mathrm{m}$. Following the same scale, the original values of Fig. 1, are divided by 12 in the model, so $D_{in} = 6.5/12\,\mathrm{m}$ and the distance between the center of outer columns is $L = 50/12\,\mathrm{m}$. Because the outer columns are the vertices of an equilateral triangle, all dimensions are sufficiently described.

Regarding the OC4-DeepCWind and its symmetry, there are three main directions that the flow can strike the platform. The first one is aligned with the x-axis 0°; the second, is 30°with the axis, which is the same as 90°; and the third is 60°with x-axis, the same as 180°. These three directions are shown in Fig. 2 by the blue arrows. Each of these directions will be simulated with different geometries represented in Fig. 3.

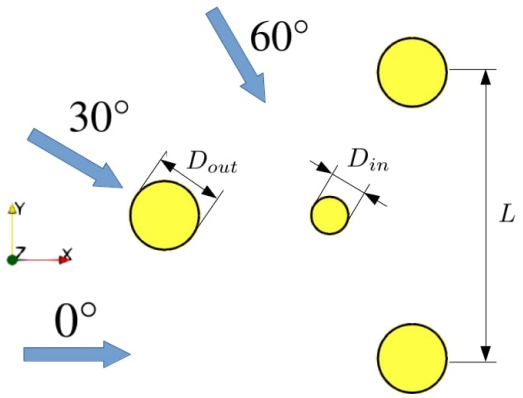

Figure 2: 2-D model of OC4 DeepCWind floating wind system.

3. METHODOLOGY

To understand the effects of VIM on the floating offshore platforms and its consequences to the wind turbine operation and mooring system performance, it is essential to accurately model this phenomenon. For numerical investigations, Computational Fluid Dynamics (CFD) is a useful tool for computing forces and visualizing the flow field.

For this purpose, simulations were performed using the finite volume method from the well-known open source CFD toolbox OpenFOAM (Weller *et al.*, 1998). We employed the version 7 provided by The OpenFOAM Foundation (OpenFOAMv7, 2019), and the mesh was built with Ansys Mesh (ANSYS, 2020).

In this work, we are interested in a first approach of the dynamic motion, so simulations were conducted using a laminar flow model with the Reynolds number defined as

$$Re = \frac{UD}{\nu} = 150,$$

where U is the inlet velocity, D is the characteristic diameter, which in this case is assumed to be the outer column diameter D_{out}, and ν is the kinematic viscosity of the fluid. For convenience, the outer diameter and inlet velocity are unitary, so the kinematic viscosity is Re^{-1}.

The 2-D floating system (Fig. 2) was modelled as a single rigid body mounted on an elastic base, firstly able to move in 1 degree of freedom, then 2-DoF, and finally 3-DoF. The first set of simulations were conducted with only 1-DoF, which was translation in the y direction, transverse to the inflow. Secondly, 2-DoF was the translation in the transverse and inline directions, the $x - y$ plane. Finally, in addition to the plane motion, the structure could rotate about the z-axis, which was the 3-DoF case. The elastic base was modelled as a linear spring of stiffness K for translation, and an axial angular spring of stiffness K_θ for rotation. The structural damping was considered null for all DoFs.

The mass ratio m^* and the reduced velocity V_r can be defined as:

$$m^* = \frac{4M}{\rho\pi D^2 l}, \qquad Vr = \frac{U}{f_n D},$$

where M is the platform mass, ρ the fluid density, D the characteristic diameter, l the column height, and f_n the natural frequency. All these values are unitary, except M ans f_n. The mass ratio was defined as m^*=2 for comparison with the single cylinder motion results from Carmo (2009), which implies that the platform model mass is $M = 5.17\,\mathrm{kg}$. The reduced velocity V_r was varied between 1 and 30, changing the natural frequency, which is defined as

$$f_n = \frac{1}{2\pi}\sqrt{\frac{K}{M}}.$$

Thus, for each reduced velocity there will be a corresponding linear stiffness K. This is the main difference from most of the experimental analysis that usually modify the reduced velocity by changing the inflow velocity U but maintaining the natural frequency f_n, thus changing the Reynolds number when the reduced velocity is varied. The values of K for each V_r simulated are shown in Tab. 1.

Table 1: Reduced velocities V_r simulated and its respective linear spring stiffness K.

V_r	1	2	3	4	5	6	7	8	9	10	11	20	30
K (N/m)	204.23	51.06	22.69	12.76	8.17	5.67	4.17	3.19	2.52	2.04	1.69	0.51	0.23

When the third degree of freedom is activated, a rotational natural frequency appears,

$$f_\theta = \frac{1}{2\pi}\sqrt{\frac{K_\theta}{I}},$$

where I is the moment of inertia of the platform, that for the 2-D model was $I = 27.88\,\mathrm{kgm}^2$. To set the torsional spring K_θ according to V_r, we fixed the ratio between the torsional and linear stiffness as:

$$\frac{K_\theta}{K} = \left(R_{zz}\frac{T}{T_\theta}\right)^2 = 0.55,$$

where $R_{zz} = I/M$ is the radius of gyration, T the natural period of linear translation, and T_θ the natural period of rotation. These values were based on the experimental model of OC4-DeepCWind (Gonçalves *et al.*, 2021).

This work analyzes the amplitudes of displacement and force in the transverse (x) and inline (y) direction by computing the root mean square (RMS) of the signal neglecting the initial transient dynamics, that is about the first 70 seconds of simulation. The assumption of a sinusoidal signal relates the amplitude and the RMS as the following:

$$A = RMS \times \sqrt{2},$$

where A is the signal amplitude, and RMS is the root mean square of the signal. With the Fast Fourier Transform (FFT), we analyzed the main frequencies of oscillation and the phase difference $\Delta\Phi$ between displacement and force.

3.1 Numerical setup

Three meshes were created, one for each flow incidence angle. They all have the same characteristics, except that in each case the platform body was rotated according to the corresponding angle, in such a way that the flow is always aligned with the x direction in the domain reference coordinate system. In Fig. 3, one can see the geometries for a flow incidence of 0°(Fig. 3a), 30°(Fig. 3b) and 60°(Fig. 3c). The domain is $L_x \times L_y = 35\,\mathrm{m} \times 30\,\mathrm{m}$. The central cylinder is placed at the origin of the coordinate system, so the inlet boundary is 15 m upstream and the outlet is 20 m downstream.

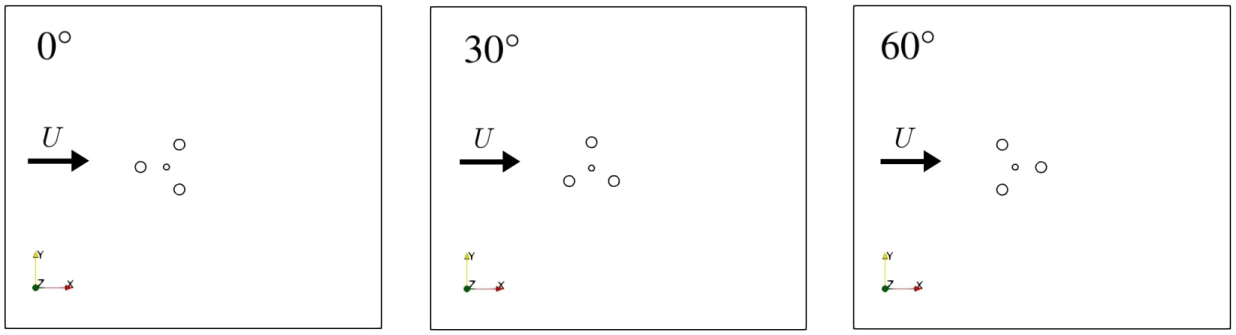

(a) (b) (c)

Figure 3: Geometries for the three main flow incidence angles: 0°(a), 30°(b) and 60°(c).

The mesh has a global growth rate between elements equal 1.1. Each cylinder is discretized in 60 elements along the perimeter and the aspect ratio of the first wall cell is 4.5. In the wake and near the structure, the elements have a maximum size of 0.2 m. The wake refinement is $10D$ width to cover the platform oscillation amplitude. Fig. 4a provides an overview of the mesh for the case of 0°, and Fig. 4b is a closer look around the cylinder vicinity. All meshes have around 14 thousand elements. To achieve this setup, several simulations were conducted in order to have a domain size and mesh resolution converged.

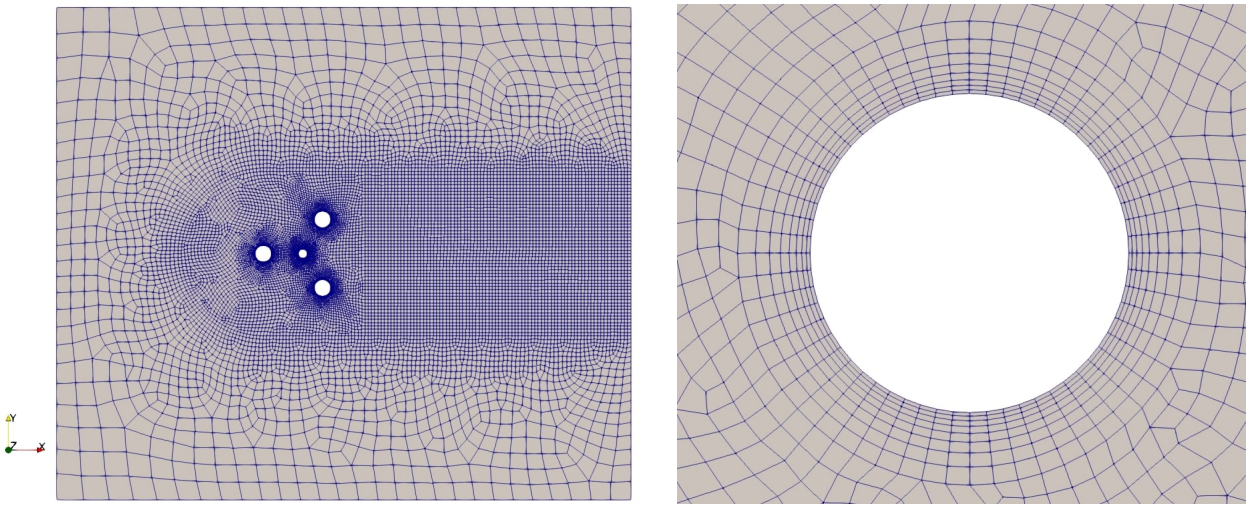

(a) Global domain (b) Cylinder vicinity

Figure 4: 2D mesh of DeepCWind platform for the case of 0°flow incidence.

The CFL condition was maintained with $Co < 1$ for a time-step $dt = 0.01$s. The y^+ is less important here because there is no turbulence model. OpenFOAM's unsteady flow solver for incompressible flows, pimpleFoam, was used with

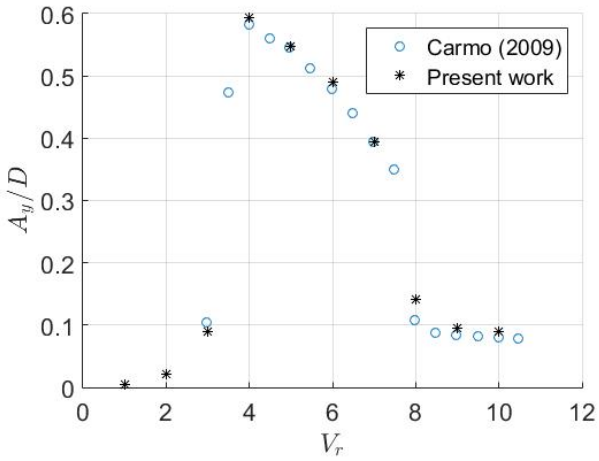

Figure 5: Validation of the 1-DoF simulation by comparing the oscillation amplitude of a single cylinder in the cross-flow direction for different reduced velocities V_r.

1st order accuracy in time (implicit Euler) and 2nd order in space. PimpleFoam combines two algorithms: PISO (Pressure Implicit with Splitting of Operator) and SIMPLE (Semi-Implicit Method for Pressure-Linked Equations). Each simulation of 400 physical seconds took approximately 1 to 2 hours of computational time in a single processor. A total of 117 (3 angles $\times$ 3 DoF $\times$ 13 V_r) cases were simulated.

Regarding the fluid structure interaction (FSI), OpenFOAM provides a dynamic mesh class named *dynamicMotionSolverFvMesh*. The solver used is the *symplectic*, a 2nd-order explicit time-integrator for 6DoF solid-body motion, that is explained in detail in Dullweber *et al.* (1997).

4. RESULTS

The first result obtained is a simple validation of the fluid structure interaction simulation at $Re = 150$. For this purpose, a 2-D cylinder restricted to oscillate only in the cross-flow direction y was simulated with the same mass ratio of the platform model m^*=2 mounted on an elastic base for reduced velocities from 1 to 11. The oscillation amplitudes show good agreement (Fig. 5) with simulation results from Carmo (2009), obtained with the spectral/*hp* element method. Since the later has nonzero damping, the results from our simulations exhibited slightly higher amplitudes.

After the validation of the vortex-induced vibration of a single cylinder, the simulations with the 2-D DeepCWind floating system model (Fig. 2) were conducted for the 3 incidence angles (0°, 30°, 60°) for 1-DoF (cross-flow translation), 2-DoF (plane translation) and 3-DoF (plane translation and rotation).

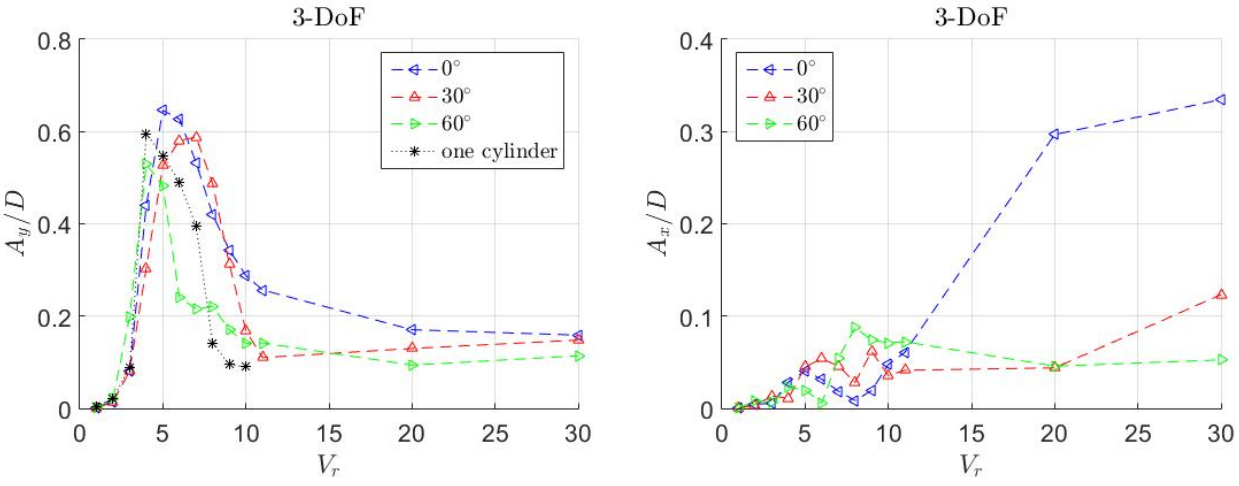

(a) (b)

Figure 6: Transverse amplitude response A_y/D for DeepCWind model compared to one cylinder (a), and the inline amplitude response A_x/D for DeepCWind model 3-DoF (b).

The amplitudes of 1-DoF cylinder are compared with 3-DoF DeepCWind model in Fig. 6a. The similarities in the behaviour of a single cylinder and the platform (4 cylinders) responses are clear. The highest peak for 0°around $0.65D$

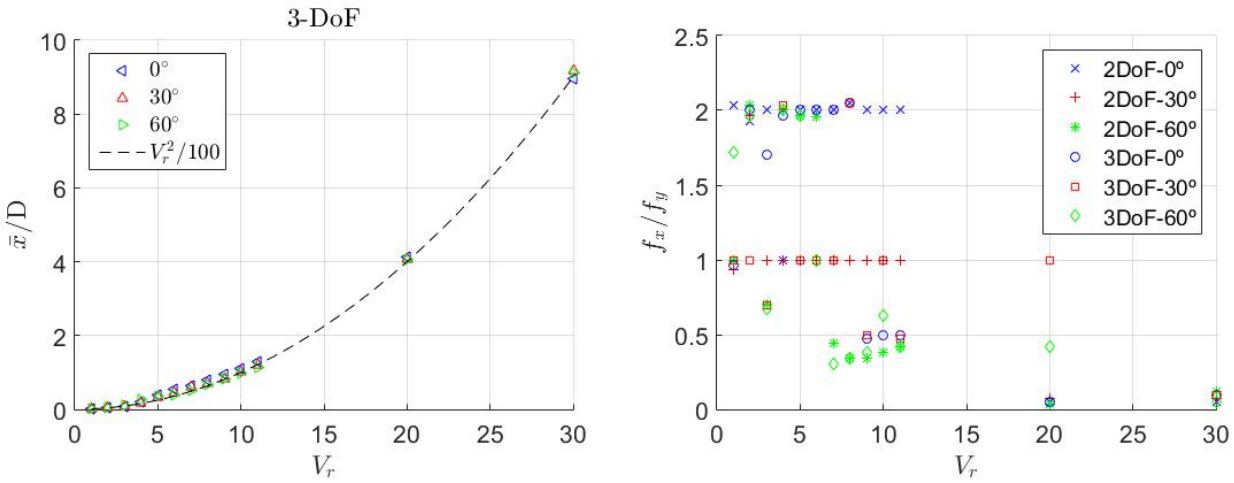

(a) (b)

Figure 7: Mean inline displacement $\bar{x}/D$ with a fit curve (a), and frequency ratio f_x/f_y between inline and transverse amplitude response.

was found in experimental data for higher Reynolds number (Gonçalves *et al.*, 2021). This experimental data also found that for 60°the peak was the lowest one, and 30°was between them. In the inline direction, Fig. 6b shows the displacement amplitude increasing with V_r and on the order of 0.1D, which is also in agreement with the experimental data. Therefore, the 2-D model in laminar regime has a good prediction for the 3-D platform in higher Reynolds.

For the largest reduced velocities (i.e., $V_r = 20$ and 30), in which the linear spring stiffness is too small, the mean x displacement of the platform is so large that the simulation diverged. To correct this issue, an initial length of the spring was set to 4 m for the case of $V_r = 20$ and 9 m for $V_r = 30$. These are approximately the mean x displacement for these cases, as it was found to follow the expression $\bar{x}/D = V_r^2/100$ (Fig. 7a), which is expected since we are employing a linear spring.

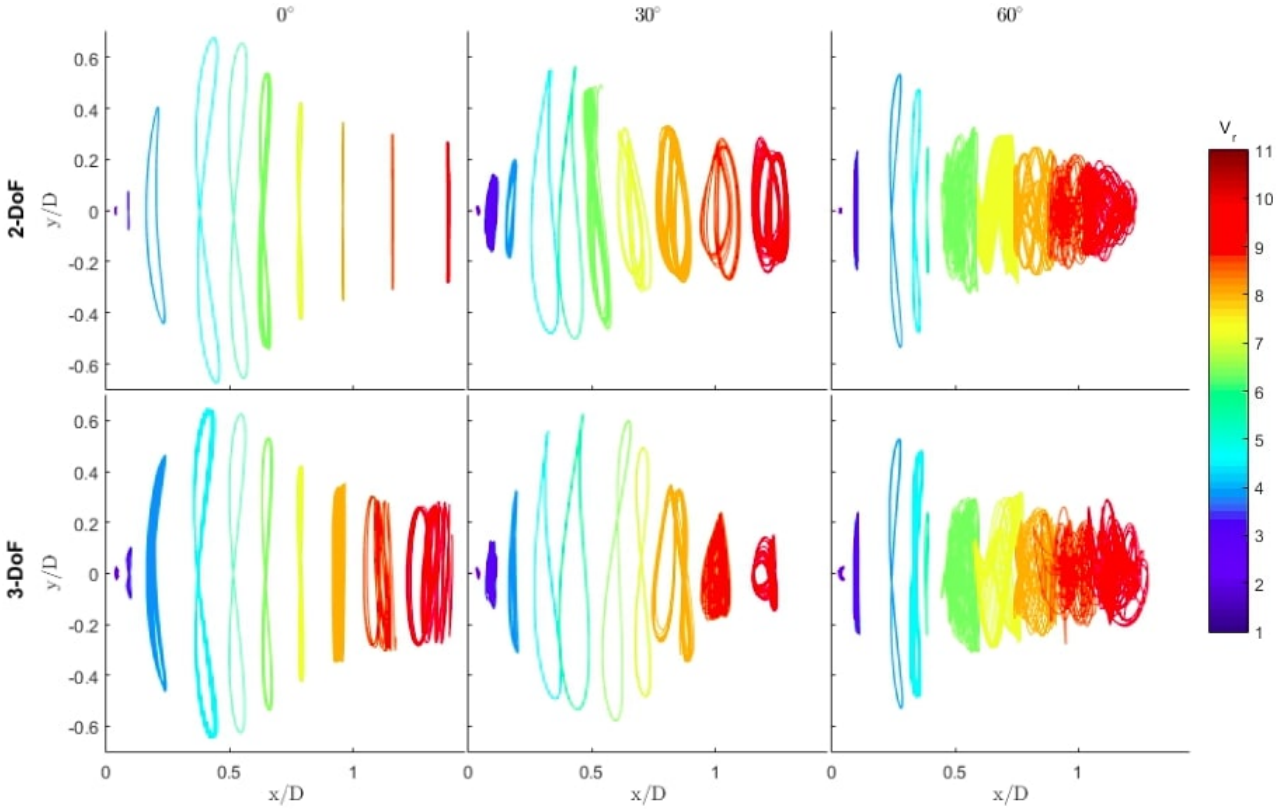

Figure 8: x-y displacement colored by the respective reduced velocity V_r for three incident flow angles (columns 0°, 30°, 60°). The first line is 2-DoF and second line 3-DoF.

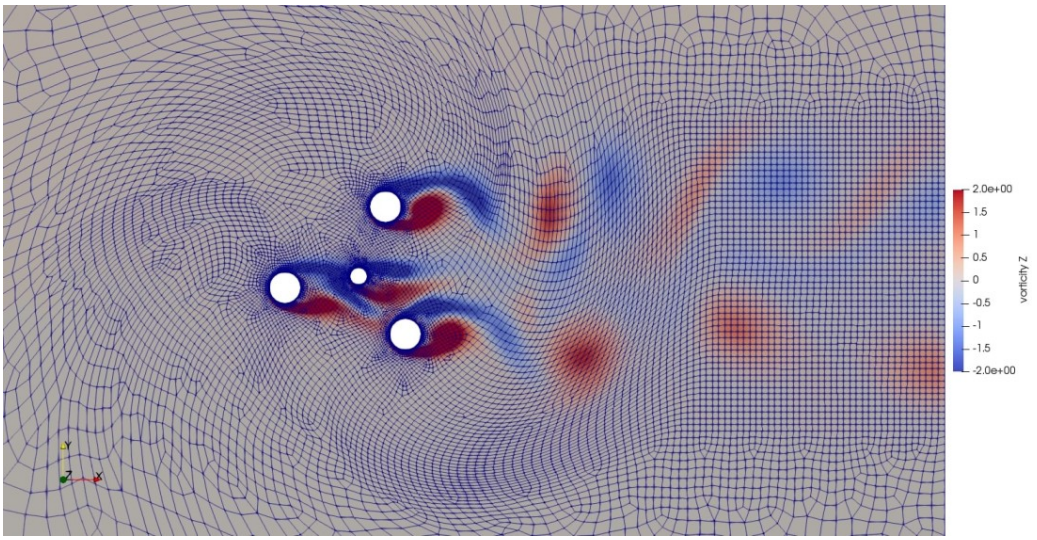

Figure 9: Mesh geometry of 60°flow incidence (Fig. 3c) turned to the stable position for $V_r = 30$. Colored by vorticity in z direction.

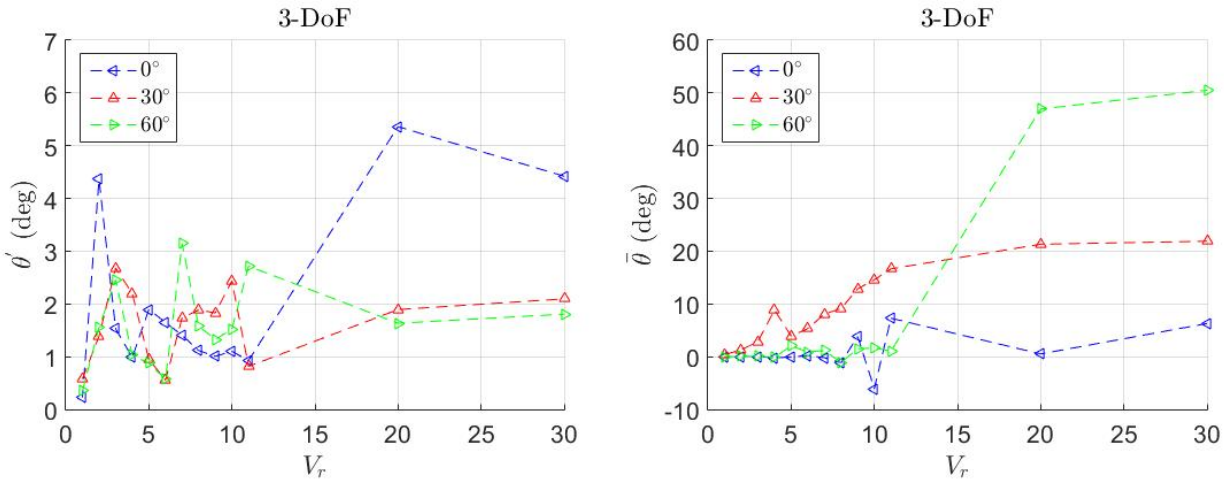

(a) (b)

Figure 10: Rotational amplitude θ' (a), and mean angle $\bar{\theta}$ (b) for the DeepCwind model 3-DoF.

Regarding the oscillation frequencies, Fig. 7b shows that the ratio f_x/f_y between inline x and transverse y response frequency has a clear tendency to be 2 for 0°(blue points) and 1 for 30°(red points). It is logical that the oscillation in one direction is related to the response in the other one. The visualization of this phenomenon is more clear in Fig. 8, where the displacement x-y of the platform for different reduced velocities is presented. In the first column (0°), it is evident the "8" path described by the body for higher amplitudes, which results in 2 oscillations in the x direction for each oscillation in the y direction. However, for the second column (30°) the figure "8" is not evident; instead, for each oscillation in y there is one in the x direction.

It is also interesting to observe in Fig. 8 how the platform motion becomes more unstable when the incident flow angle increase. In the first line (2-DoF), for the 0°case, the trajectories are well defined, for 30°, the trajectories are less ordered, and finally, for 60°, the paths are very disordered, mainly for higher V_r.

The instability at 60°is well observed for the highest reduced velocity V_r=30, which means the lowest stiffness. In this case, a 3-DoF simulation results in a mean displacement angle $\bar{\theta}$ near to 60°, which means that the platform turns to the more stable position of 0°flow incidence. In the simulation, this means a mesh turning of almost 60°, which can be visualized in Fig. 9, colored by vorticity. Fortunately, the mesh had a good behavior despite the high distortions. One can observe the rotation by comparing the initial geometry (Fig. 3c) with the final result (Fig. 9).

Fig. 10b presents the mean angle $\bar{\theta}$ for all cases simulated in 3-DoF. It is possible to observe that the green curve tends to 60°, and the red curve tends to 30°for high V_r (low spring stiffness). It is easy to demonstrate that, if a constant drag force is applied equally to all platform columns, the resultant torque is null and the θ angle is neutrally stable. In other words, it will not rotate, unless transient effects and interactions between cylinders arise.

For the 60°geometry (Fig. 3c), the downstream cylinder is on the wake of the central cylinder. This implies a lower drag on the downstream cylinder and thus, an unstable position. Similar behaviour occurs for the 30°geometry (Fig. 3b), where the downstream cylinder is in the wake of the upstream cylinder. The only position that the outer columns do not experience strong wake effects is the 0°geometry (Fig. 3a), where only the central cylinder is strictly on the wake of the upstream cylinder. Therefore, this is the most stable configuration.

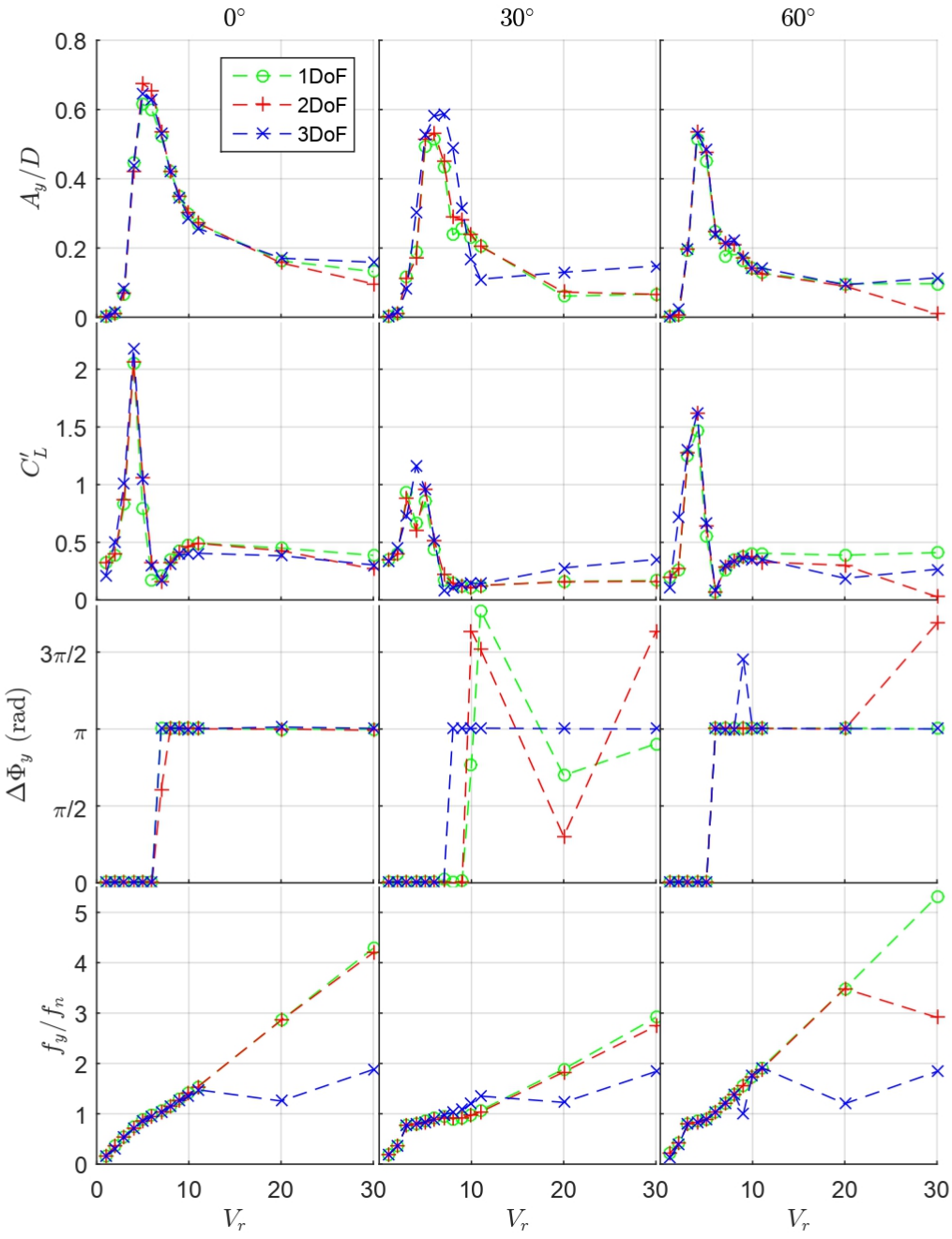

Figure 11: Oscillation amplitude A_y/D, force amplitude $C_L{}'$, phase difference $\Delta\Phi_y$ between them, and the ratio f_y/f_n between oscillation frequency and natural frequency. All with respect to the transverse flow direction. Each column is a flow incidence angle and colors represent the degrees of freedom (DoF).

In addition, comparisons between the different degrees of freedom are presented in Fig. 11 and Fig. 12. The first line of Fig. 11 shows good agreement between different DoFs for the transverse amplitude response A_y/D, except for 30°, in which the 3DoF blue curve is slightly detached. One can also observe the decrease of peak amplitude with increasing angle, which was already shown in Fig. 6a. The second line presents the transverse force amplitude $C_L{}'$, that has the lowest peak for the 30°cases, and for the other angles has a good agreement between the DoF's. One must remark that

for a specific reduced velocity (7 for 0°and 30°, and 6 for 60°) this force is approximately zero. This happens because the forces on each cylinder are in counter phase and annul each other. This is related to the third line, that represents the phase difference $\Delta\Phi_y$ between transverse displacement and force. It is ease to notice that the phase shift from 0 to π takes place when the lower ${C_L}'$ occurs. Finally, the last line of Fig. 11 present the transverse amplitude frequency f_y compared to its natural frequency f_n, and there is a clear linear behaviour for $f_y/f_n > 1$, despite the fact that the blue curves detach for higher V_r.

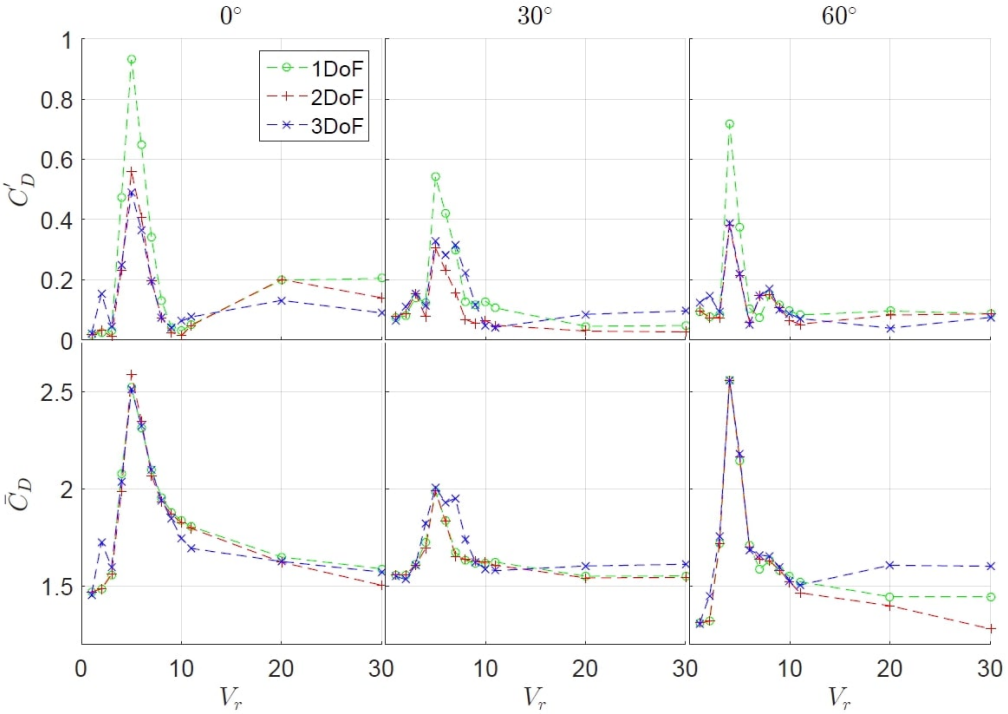

Figure 12: Amplitude ${C_D}'$ of the dimensionless inline force and its mean value $\bar{C}_D$. Each column is a flow incidence angle (0°, 30°, 60°) and colors represent the degrees of freedom (DoF).

In Fig. 12, the amplitude of the streamwise force ${C_D}'$ and its mean value $\bar{C}_D$ are presented. In the first line, the ${C_D}'$ peak is higher for 1-DoF, in the second line there is a good agreement between different DoF's, and one can notice that for 30°the mean force $\bar{C}_D$ is lower because the downstream outer cylinder is in the wake of another outer cylinder. For the 3-DoF simulations, forces, amplitudes, and frequencies of the 3 inflow angles converge roughly to the same value at higher V_r because all initial angles turn approximately to the same incidence angle 0°as presented in Fig. 9.

5. CONCLUSIONS

The present work simulated the VIM phenomenon of an offshore wind floating system modelled in 2-D geometry for 1, 2, and 3 degrees of freedom on the plane. The flow regime was laminar and reduced velocities were tested from 1 to 30 by changing the elastic base stiffness. The results showed good agreement with experimental data for a 3-D model in higher Reynolds number for inline and transverse amplitude response.

It was found that the mean inline displacement varies with $V_r^2/100$ and there is a lock-in ratio frequency of 2 or 1 between inline and transverse response according to the inflow angle. This is related to whether the "8-path" is described by the structure or not. The trajectories showed that 0°inflow angle is the most stable position, and 60°the most unstable. Torque analysis on the outer cylinders showed that fluid interference is responsible for this instability angle.

The differences between the number of degrees of freedom are small for displacement amplitudes, mean forces, and frequencies, for low to moderate reduced velocities. For 30°, the rotational freedom is more important and differs from 1-DoF and 2-DoF results. Finally, the inline force amplitude was found to be overestimated when only 1-DoF is activated.

This work shows that reliable results are obtained with a simple 2-D model in the laminar regime. It helps to understand the interaction between columns in the offshore context and allows researchers to better model the VIM phenomenon.

6. ACKNOWLEDGEMENTS

This work was developed as part of the R&D project conducted by Petrobras and the University of São Paulo entitled "Research and Development on Deep Water Floating Offshore Wind Turbines" (agreement Petrobras #5900.0112605.19.9). Authors wish to thank Petrobras for the funding of this project and the Brazilian National Petroleum Agency (Agência

Nacional do Petróleo, ANP) for providing the regulatory framework under which this funding occurs. B. S. Carmo acknowledges financial support from the Brazilian National Council for Scientific and Technological Development (CNPq) in the form of a productivity grant (grant number 312951/2018-3). The simulations were run using the computational infrastructure of the Centre of Dynamics and Fluids (NDF) of Escola Politécnica, University of São Paulo.

7. REFERENCES

ANSYS, 2020. "Ansys meshing, ansys inc." `https://www.ansys.com/products/meshing`.

Carmo, B.S., 2009. "On wake interference in the flow around two circular cylinders: direct stability analysis and flow-induced vibrations".

Dullweber, A., Leimkuhler, B. and McLachlan, R., 1997. "Symplectic splitting methods for rigid body molecular dynamics". *The Journal of chemical physics*, Vol. 107, No. 15, pp. 5840–5851.

Esteban, M.D., Diez, J.J., López, J.S. and Negro, V., 2011. "Why offshore wind energy?" *Renewable Energy*, Vol. 36, No. 2, pp. 444–450.

Fujarra, A.L., Rosetti, G.F., de Wilde, J. and Gonçalves, R.T., 2012. "State-of-art on vortex-induced motion: A comprehensive survey after more than one decade of experimental investigation". In *International Conference on Offshore Mechanics and Arctic Engineering*. American Society of Mechanical Engineers, Vol. 44915, pp. 561–582.

Gonçalves, R.T., Chame, M.E., Silva, L.S., Koop, A., Hirabayashi, S. and Suzuki, H., 2021. "Experimental flow-induced motions of a fowt semi-submersible type (oc4 phase ii floater)". *Journal of Offshore Mechanics and Arctic Engineering*, Vol. 143, No. 1, p. 012004.

Johlas, H.M., Martínez-Tossas, L.A., Churchfield, M.J., Lackner, M.A. and Schmidt, D.P., 2021. "Floating platform effects on power generation in spar and semisubmersible wind turbines". *Wind Energy*.

OpenFOAMv7, 2019. "The openfoam foundation, openfoam v7". `https://openfoam.org/version/7/`.

Robertson, A., Jonkman, J., Masciola, M., Song, H., Goupee, A., Coulling, A. and Luan, C., 2014. "Definition of the semisubmersible floating system for phase ii of oc4". doi:10.2172/1155123. URL `https://www.osti.gov/biblio/1155123`.

Weller, H.G., Tabor, G., Jasak, H. and Fureby, C., 1998. "A tensorial approach to computational continuum mechanics using object-oriented techniques". *Computers in physics*, Vol. 12, No. 6, pp. 620–631. doi:10.1063/1.168744.

8. RESPONSIBILITY NOTICE

The authors are solely responsible for the printed material included in this paper.